Numerical analysis of multi-modal vibrations of a vertical riser in step currents

Yu Duanmu [a,b], Lu Zou [a], Decheng Wan [a,*]

[a] Collaborative Innovation Center for Advanced Ship and Deep-Sea Exploration, State Key Laboratory of Ocean Engineering, School of Naval Architecture, Ocean and Civil Engineering, Shanghai Jiao Tong University, Shanghai, 200240, China
[b] Guangzhou Maritime University, Guangzhou, 510725, China

ABSTRACT

This paper describes numerical simulations of the vortex-induced vibrations (VIVs) of a long flexible riser in a step current. We consider the model vertical riser tested at the Delta Flume. The simulation is carried out by our in-house computational fluid dynamics (CFD) solver viv-FOAM-SJTU, which was coupled with the strip method and developed in OpenFOAM platform. The vibration modes in both in-line (IL) and cross-flow (CF) directions are accurately predicted. The numerically predicted maximum mean IL displacement and its location differed marginally from the experimental results. The good agreement between the numerical and experimental results proved that this solver was reliable for predicting the VIV response. A large number of numerical tests were then carried out to study the effects of various parameters on VIV responses further. Three main parameters are considered in this study: current velocity, top tension and mass ratio. The intrinsic relationship between the natural frequency and oscillating frequency was analyzed to explain the occurrence of the dominant mode. Based on the numerical results, the regular characteristics of the VIV response with the reduced velocity were pointed out. The curvatures and the maximum mean offset values were proportional to the squares of the reduced velocities.

1. Introduction

Vortex-induced vibration (VIV) is a critical concern for the offshore industry; it affects pipelines, spar platforms and risers. The greatest concern of those is in the field of deep-water oil extraction. Recently, offshore oil platforms have been installed in water depths of over 2000 m. As a result, there is a great need to develop a reliable numerical solver for the prediction of VIV response of risers with very high aspect ratios.

Over the past few decades, VIV responses of long flexible risers have been extensively studied. Model testing has given valuable insights into the phenomenon of VIVs (Chaplin et al., 2005a, 2005b; Huera Huarte, 2006; Huera-Huarte et al., 2006; Huera-Huarte and Bearman, 2009a, 2009b). These model tests have shown that the response included significant contributions from several modes except at the lowest reduced velocities; a temporary mode transition could also occur occasionally. Apart from the experimental studies, numerical investigations have also attracted the attention of researchers. Empirical models and CFD models are the two main numerical methods used to predict the vibrations of risers (Willden and Graham, 2001, 2004, 2006; Srinil, 2010; Duan and

Wan, 2016a; Duan et al., 2016). Willden and Graham (2004) investigated the transverse VIVs of a flexible riser with an aspect ratio of the order of 1000. It has been observed that the mode of vibration with frequency closest to the local natural vortex shedding frequency is most likely to be excited. Wang and Xiao (2016) presented a numerical study on VIVs of a vertical riser subject to uniform and linearly sheared currents. The IL and CF vibrations were predicted accurately. Zhang et al. (2017) presented a systematic study of the flow around a spring mounted wavy cylinder mainly at a moderate Reynolds number of 5000. Borazjani and Sotiropoulos (2009) investigated VIVs of two identical 2D elastically mounted cylinders in tandem in the proximity-wake interference regime at $Re = 200$ for systems having one and two degrees of freedom. Zhao and Wan (2016a, 2016b) studied flow past a cylinder and two cylinders by the approaches of SST-DES and SST-DDES.

Chaplin et al. (2005a) compared laboratory measurements of the VIV responses of a riser with the blind predictions obtained via 11 different numerical methods, including six CFD models and five empirical models. It was found that the empirical models were more successful at predicting CF displacements than CFD models. However, the mode transition of the

Nomenclature

ϕ^m	Modal shape of the mth mode	m_x	In-line mode number
c_x	In-line curvature	m_y	Cross-flow mode number
c_y	Cross-flow curvature	$\bar{s}$	Time-averaged value of the variable s
D	Diameter of the riser	σ_s	Standard deviation of the variable s
f_n^m	Natural frequency of mth mode	s^{max}	Maximum value of the variable s over elevation z
f_S	Vortex shedding frequency	s_{rms}	Root mean square value of the variable s over elevation z
f_{ox}	In-line oscillatory frequency	St	Strouhal number
f_{ox}^m	In-line oscillatory frequency of mth mode	T_t	Top tension of the riser
f_{oy}	Cross-flow oscillatory frequency	u^m	In-line modal weight of mth mode
f_{oy}^m	Cross-flow oscillatory frequency of mth mode	v^m	Cross-flow modal weight of mth mode
L	Length of the riser	V_r	Reduced current velocity
m	Mode number	x	In-line displacement
m^*	Mass ratio	y	Cross-flow displacement
		z	Elevation

response with respect to time could not be embodied in those empirical models; mode transition is a key feature of VIV responses of long flexible risers. However, the IL responses obtained by the given six CFD models were not in agreement with the experimental results. Thus, there is need for improvement in the accuracy of the CFD model.

The dynamic features of long slender cylinders are determined by many structural parameters. The vibration amplitudes and modes of riser VIV responses are also influenced by the flow field. Using experimental, numerical and empirical models, many researchers have addressed this very important topic. Chaplin et al. (2005b) presented an experimental study of a vertical model riser with a different top tension, which was exposed to a stepped current. In the experiment of Huera-Huarte and Bearman (2009a), three different top tensions were investigated. For the smallest top tension, the initial, lower and upper branches were observed in the dynamic response of the model, whereas for the other top tension cases, the lower branch of the dynamic response vanished. Chen et al. (2012) investigated the dynamic characteristics and VIVs of the deep-water riser with axially varying structural properties. Huang et al. (2011) investigated cases that covered a wide range of riser VIV problems for risers having different outer diameters, lengths, tensioning conditions and current profiles.

For risers having such high aspect ratios and complex flow fields around them, a complete three-dimensional simulation is not feasible. The strip theory is an efficient strategy for solving VIV problems of flexible cylinders with extremely high aspect ratios. Based on the strip theory, we developed the solver viv-FOAM-SJTU by using the open source code package, OpenFOAM. The entire fluid-structure solution procedure was carried out in the time domain via a loose coupling strategy. We applied the mesh movement based on interpolation using the radial basis function (RBF). The solver has good versatility; it allows simulations of VIVs in both CF and IL directions with various aspect ratios, mass ratios, top tensions and current profiles.

To validate the solver, we carried out numerical simulations of the VIVs for the benchmark case. The numerical results were found to be in good agreement with the benchmark data given in Huera-Huarte (2006). Based on the study of the flow field, the intrinsic relationship between the flow field and the vibration response of the riser was analyzed. The main contribution of this paper is that it investigates the parametric effects on the VIV based on the solver viv-FOAM-SJTU. A series of test studies are conducted using different parameters. The effects of top tension, current velocity and mass ratio are investigated, and the response modes and trends analyses under different conditions are presented. The results show multi-mode characteristics of vibrations of the riser.

The rest of the paper is organized as follows. A brief introduction to the numerical methods is given in Section 2. In this section, the governing equations of flow field and structure field are introduced. The detailed algorithm of the fluid-structure interaction strategy is presented. In addition, the post-processing method of displacement responses is presented for modal analyses. In Section 3, the computations are validated by comparison with the benchmark experiment of Huera-Huarte (2006). Section 4 provides a detailed study of the effects of different parameters on VIV. The parameter analysis of the current velocity, the top tension and the mass ratio are investigated separately. In section 5, the study of the VIV responses with respect to the reduced velocity based on the previous results are presented. We analyzed the changes in the standard deviations of the displacement and the curvature as the velocity is reduced. Finally, in the last section, conclusions are drawn based on the results presented.

2. Method

2.1. Flow model

The flow field is modelled by solving the unsteady, incompressible Reynolds-averaged Navier-Stokes (URANS) equations

$$\nabla \cdot \boldsymbol{U} = 0 \tag{1a}$$

$$\rho \frac{\partial \boldsymbol{U}}{\partial t} + \rho \nabla \cdot \left((\boldsymbol{U} - \boldsymbol{U}_g) \boldsymbol{U} \right) - \nabla \cdot \left(\mu_{eff} \nabla \boldsymbol{U} \right) - (\nabla \boldsymbol{U}) \cdot \nabla \mu_{eff} = -\nabla p_{eff} \tag{1b}$$

where $\boldsymbol{U}$ is the flow velocity and $\boldsymbol{U}_g$ is the grid velocity, $\mu_{eff} = \rho(\nu + \nu_t)$ the effective dynamic viscosity, in which ν and ν_t are mixture kinematic viscosity and eddy viscosity, respectively. ν_t is obtained by the SST turbulence model for turbulence closure. $p_{eff} = p + {}^2\!/\!{}_3 \rho k$ is the effective pressure, in which k is the turbulence kinetic energy.

2.2. Structural dynamic model

A finite element structural model based on the Euler-Bernoulli beam theory is employed to calculate the dynamic response of the cylinder. Supposing that EI and m^* remain constant along the span, we have

$$EI \frac{\partial^4}{\partial z^4} x(z,t) - \frac{\partial}{\partial z}\left[T(z) \frac{\partial x(z,t)}{\partial z} \right] + m \frac{\partial^2 x(z,t)}{\partial t^2} + c \frac{\partial x(z,t)}{\partial t} = f_x(z,t) \tag{3a}$$

$$EI \frac{\partial^4}{\partial z^4} y(z,t) - \frac{\partial}{\partial z}\left[T(z) \frac{\partial y(z,t)}{\partial z} \right] + m \frac{\partial^2 y(z,t)}{\partial t^2} + c \frac{\partial y(z,t)}{\partial t} = f_y(z,t) \tag{3b}$$

The axial force of the pipe $T(z)$ varies spatially, but not temporally, because of the effects of the weights. To solve the structural dynamic equations in Finite Element Methods (FEMs), Eq. (3a) and Eq. (3b) can be

discretized as

$$[M]\{\ddot{x}\} + [C]\{\dot{x}\} + [K]\{x\} = \{F_x\},$$

$$[M]\{\ddot{y}\} + [C]\{\dot{y}\} + [K]\{y\} = \{F_y\},$$

where $\{x\}$ and $\{y\}$ are the nodal displacement vectors and with dots denoting differentiation with respect to time, $[M], [C]$ and $[K]$ are the mass, damping and stiffness matrices, respectively. $\{F_x\}$ and $\{F_y\}$ are the hydrodynamic force vectors. The governing equations are solved using the Newmark-beta method.

2.3. Fluid-structure interaction

The strip theory CFD model is used to simulate the fluid dynamics. The fluid flow computed locally in multiple two-dimensional computational planes is placed along the cylinder span. The PIMPLE (merged PISO-SIMPLE) algorithm in OpenFOAM is adopted to compute the flow field, which is appropriate for solving the transient incompressible problem. The reliability of this locally two-dimensional method has already been confirmed (Willden and Graham, 2004).

The fluid force at the individual axial strips is mapped to the nodes of the structural model at the start of each time step. Subsequently, the pipe's motion is computed based on the Euler-Bernoulli beam theory, and the motion is used for moving the boundaries in the fluid domain accordingly. Then, the computation of a new flow field is followed. In this way, a time step is advanced. This procedure is shown in Fig. 1. Based on the above theory the solver viv-FOAM-SJTU was developed. The entire flow-structure solution procedure was carried out in the time domain by using a loose coupling strategy.

2.4. Mesh deformation based on the RBF method

The viv-FOAM-SJTU solver applies the radial basis function (RBF) dynamic grid technique into solution of dynamic mesh of OpenFOAM. The RBF dynamic grid technique could facilitate large mesh deformation that limits the application of Laplace mesh deformation. The viv-FOAM-SJTU solver could predict the VIV responses in both IL and CF directions of flexible riser with aspect ratio of 1000 magnitude under high Reynolds number.

It is always expected to find a mesh solution method that is not only efficient and capable of enduring large mesh deformation, but also maintain the quality of the grid after deformation (especially the grid in

Fig. 1. Fluid-structure interaction.

the boundary layer). The solution that can meet the above three demands are achieved by the RBF grid technique. If the inner and outer diameters are set appropriately, the grid inside the boundary layer could keep relatively static, and the mesh quality and the deformation ability of the mesh will also be secured.

The RBF dynamic grid technique based on the dynamic mesh module (dynamicFvMesh) of OpenFOAM is developed. The RBF interpolation, which is first proposed by Rendall and Allen (2008), can be used to derive the displacement of the internal fluid nodes when the displacement of the structural nodes on the interface is given.

The RBF is a set of basis functions with Euclidean distances defined as follows:

$$s(r) = \sum_{i=1}^{n} \gamma_i \phi(r)$$

where r is the Euclidean distance, and $\phi(r)$ is the general form of the RBF function which has various forms. There are four commonly used functions: C2, TPS, Gauss and IMQB; the definitions of these functions are given in Table 1. The parameter γ_i is the interpolation weight coefficient for the interpolation point i, and n is the number of the object surface nodes of the dynamic mesh.

2.5. Post processing

Following Chaplin et al. (2005b), the IL and CF deflections of the riser from the initial vertical straight-line condition were denoted by $x(z, t)$ and $y(z, t)$, respectively.

The deflected shape of the riser can be usefully represented in spectral terms, which means that each pipe's total displacement can be decomposed into modal contributions. The displacements in IL and CF directions can then be expressed in terms of time-dependent modal weights $\mathbf{u} = (u^1, u^2, ..., u^M)$ and $\mathbf{v} = (v^1, v^2, ..., v^M)$ as

$$x(z, t) = \sum_{m=1}^{M} \phi^m(z) u^m(t) \tag{4a}$$

$$y(z, t) = \sum_{m=1}^{M} \phi^m(z) v^m(t) \tag{4b}$$

where $\phi = (\phi^1, \phi^2, ..., \phi^M)$ is the matrix of the mode shapes, and M is the number of unconstrained structural degrees of freedom.

The matrix form of Eq. (4) is

$$\mathbf{x}(z, t) = \phi(z)\mathbf{u}(t) \tag{5a}$$

$$\mathbf{y}(z, t) = \phi(z)\mathbf{v}(t) \tag{5b}$$

The required mode is only needed to solve. The least squares method is needed to solve the equations. In this way, the required modal information is achieved and the rest mode is filtered out. The numpy library of python is used to solve the equations.

Spatial frequency analysis can also be performed over the curvatures. Let us take the second derivative of Eq. (4) and assume that $[\phi^m(z)]'' = -k^2 m^2 \phi^m(z)$ is satisfied, where k is some constant, that is, the mode shapes are exactly sinusoidal or something similar. Therefore, we have
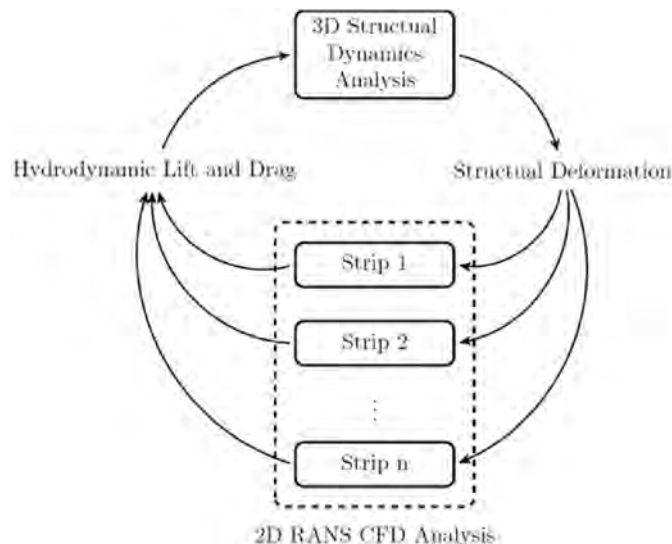
Table 1
Definition of radial basis functions.

No	Name	Abbreviation	$f(x)$
1	Wendland's C2	C2	$(1-r)^4(4r+1)$
2	Thin Plate Spline (TPS)	TPS	$r^2 \log(r)$
3	Gaussian	Gauss	e^{-r^2}
4	Inverse multiquadric biharmonics	IMQB	$\sqrt{\frac{1}{a^2+r^2}}$

$$c_x(z,t) = x''(z,t) = \sum_{m=1}^{M} -k^2 m^2 \phi^m(z) u^m(t) \qquad (6a)$$

$$c_y(z,t) = y''(z,t) = \sum_{m=1}^{M} -k^2 m^2 \phi^m(z) v^m(t) \qquad (6b)$$

where a prime sign denotes differentiation with respect to z; $c_x = x''/(1 + x')^{3/2} \approx x''$ is considered suitable for this study because x' is always far below 1. This is also suitable for c_y. Thus, the modal weights for the curvature $-k^2 m^2 u^m$ and $-k^2 m^2 v^m$ can be of high absolute value for a large mode number.

We know from Lie and Kaasen (2006) that the modal responses that are physically impossible to be included in the observed range of responses should be excluded from the analysis. However, if those undesirable mode shapes are discarded just after solving Eq. (5), some information useful to the remaining accepted mode-shapes may also be discarded. Taking this into account, Lie and Kaasen (2006) chose to solve the modal amplitudes in the least-squares sense. Consequently, the time histories of the modal displacements for each spacing was obtained at every time step as

$$\phi^T(z) \boldsymbol{x}(z,t) = \phi^T(z) \phi(z) \boldsymbol{u}(t)$$

$$\phi^T(z) \boldsymbol{y}(z,t) = \phi^T(z) \phi(z) \boldsymbol{v}(t)$$

where only the desirable mode shapes are included in ϕ.

3. Validation of computations

The validation of the solver viv-FOAM-SJTU follows Huera-Huarte (2006) benchmark experiments; the experimental setup is shown in Fig. 2.

The model riser and experimental setting are the same as that of Chaplin et al. (2005a, b), with key parameters set out in Table 2.

A series of simulations of the model riser has been undertaken; the riser was 28 mm in diameter, 13.12 m in length and had a bending stiffness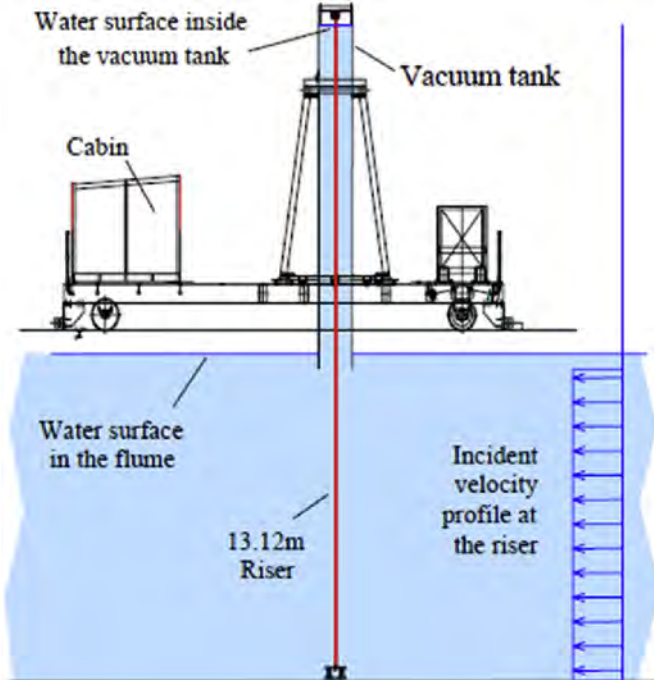 of 29.88 Nm^2; the lower 45% of the riser was exposed to a uniform current whereas the upper part remained in still water.

3.1. Natural frequency

The natural frequency is obtained as follows:

$$(\boldsymbol{K} - \lambda \boldsymbol{M})\phi = 0 \qquad (7)$$

where $\boldsymbol{K}$ and $\boldsymbol{M}$ are the stiffness matrix and mass matrix, respectively; λ is a diagonal matrix consisting of $\lambda_{ii} = \omega_i^2$, where ω_i is the natural frequency of the system.

The FEM calculation of the natural frequencies related to the first ten modes of the riser are presented. The FEM natural frequencies and mode shapes are shown in Table 3 and Fig. 3. Here the top tension is taken as 1600 N. The experimental natural frequencies are shown in Table 4. The riser was excited after setting different top tensions to determine the experimental natural frequencies. Twelve sets of tests were carried out. The top tensions were increased from 397 N to 1919 N, and the closest one was 1676 N. Table 4 gives the first ten experimental natural frequencies at the top tension of 1676 N.

The mode shapes can be quite similar to pure sinusoids. The mass ratios are of small values; therefore, tension variations along the riser span become insignificant. These results lay the foundation for subsequent studies on multi-mode vortex-induced vibrations of the riser.

3.2. Numerical model and boundary conditions

Fig. 4 shows the distribution of 20 strips placed at equal distances along the portion of the riser exposed to a uniform current. No strip is placed on the upper part, which is in still water. The riser is discretized into 90 equal structural elements. Forty elements are placed on the lower part in the uniform flow. For each element of this part, a distributed load is applied. The remaining 50 elements are placed on the upper part in the still water.

The computational mesh of each strip is shown in Fig. 5. The boundary conditions are given as follows:

The inlet velocity boundary conditions are set to be the same as the freestream velocity:

$$u = u_0, \quad v = w = 0$$

The outflow boundary condition is defined by:

$$\frac{\partial u}{\partial x} = \frac{\partial v}{\partial x} = \frac{\partial w}{\partial x} = 0$$

The symmetry boundary condition is applied to other sides of the domain to avoid the effect of the boundaries on the flow field:

$$\frac{\partial U}{\partial y} = \frac{\partial W}{\partial y} = 0, \quad V = 0$$

The no-slip boundary condition is employed at the surface of the cylinder. The velocity of the cylinder boundary must agree with the pipe motion calculated using the 3D FEM structural analysis:

$$\boldsymbol{u} = \boldsymbol{u}_{solid}$$

Fig. 2. Layout of the experiment of Huera-Huarte (2006).

Table 2
Key parameters for the benchmark experiment.

	Symbol	Value	Unit
Mass ratio	m^*	3.0	–
Current velocity	V	0.6	ms^{-1}
Diameter	D	0.028	m
Submerged length	L_s	5.94	m
Total length	L	13.12	m
Flexible stiffness	EI	29.88	Nm^2
Top tension	T_t	1600	N

Table 3
First ten FEM natural frequencies (unit: Hz).

f_1	f_2	f_3	f_4	f_5	f_6	f_7	f_8	f_9	f_{10}
1.224	2.452	3.688	4.936	6.201	7.487	8.796	10.233	11.520	12.906

3.3. Cross-flow motion analysis

The displacements have been decomposed into modal contributions to manifest the modal feature, especially the multi-mode feature. Fig. 6 depicts the modal amplitudes from the 2nd to the 7th non-dimensional CF displacement; it also shows the power spectral densities of modal weights. The dynamics in the CF direction are governed by the 4th mode response. The 4th mode response appears to be the most energetic, as seen from its modal power spectral density. The CF modal analysis agrees well with the experimental data, as shown in Fig. 7. There is evidence of simultaneous contributions from the modes on either side of the dominant 4th mode. The power spectral densities of the left modes are very small; therefore, their modal contributions to the total mode shape can be neglected. The modal amplitude of this study is not as stable as the experimental results; its Reynolds number is approximately 1.69×10^4. At this Reynolds number, the flow is fully turbulent. The turbulence is irregular, multi-scale and non-linear. In Huera-Huarte (2006), the modal amplitudes of different serial experiments were found to be quite stable. It is possible that a device might have been installed to stabilize the vibration of the riser. However, the modulating responses in the CFD simulations that come from the numerical aspects also account for this stability.

Next, we proposed an analysis of the dominant mode. The vibration frequency of riser was obtained by performing a fast Fourier transform (FFT) of the CF displacement modal amplitudes. On the right of Fig. 6 is the power spectra of the CF displacement modal amplitudes. The frequency corresponding to the dominant mode is equal to 4.556 Hz. This value is very close to the 4th natural frequency. Consequently, the CF vibration is controlled by the 4th mode. It is also worth noting that the dominant frequency width is considerably wider than that of the experimental data; therefore, one may expect more than one mode modulation during the vibration.

Typical instantaneous deflected shapes of the riser and the relevant experimental results are shown in Fig. 8 (a) and Fig. 8 (b), where the CF displacements are plotted against the relative elevation z/L. Continuous lines in Fig. 8 (a) plot the positions of the riser at intervals of 0.01 s through a time period (1 s) of the CF oscillation. The numerical results agree well with the experimental data (see Fig. 8 (b)) not only in the mode shape but also in the predicted amplitude. The saddle points of the numerical deflected shapes are fixed and distributed at equal distances
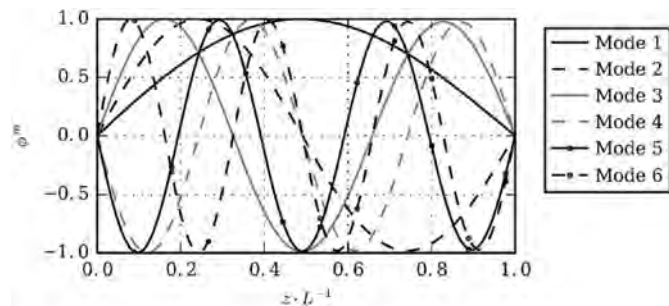
along the riser. A typical feature of the results is demonstrated in Fig. 8—the displacements of the upper part of the riser (in still water) are not smaller than those exposed to the uniform flow below because the oscillation of the riser is excited at the lower half of the riser, and the vibration wave propagates from the bottom to the top.

Fig. 9 (a) shows the spatio-temporal plot of the non-dimensional CF responses, obtained by numerical simulation. It shows that the dominant mode shape is controlled by the 4th mode, which agrees well with the

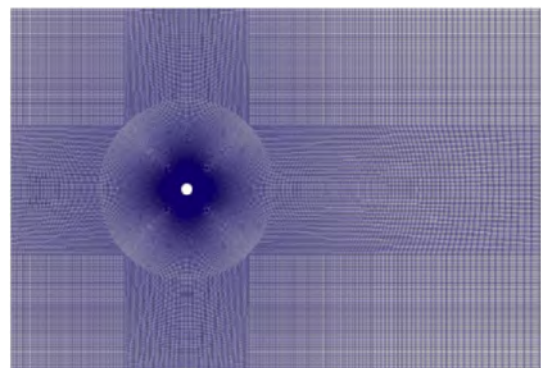**Fig. 4.** Illustration of multi-strip model.

Fig. 5. Domain and mesh of a strip.

Fig. 3. Modal shape of first 5 modes for displacement obtained from FEM.

Table 4
First ten experimental natural frequencies (unit: Hz).

f_1	f_2	f_3	f_4	f_5	f_6	f_7	f_8	f_9	f_{10}
1.223	2.414	3.657	4.855	6.120	7.855	8.632	9.941	11.301	12.595

ARTICLE IN PRESS

Y. Duanmu et al.   Ocean Engineering xxx (2017) 1–15
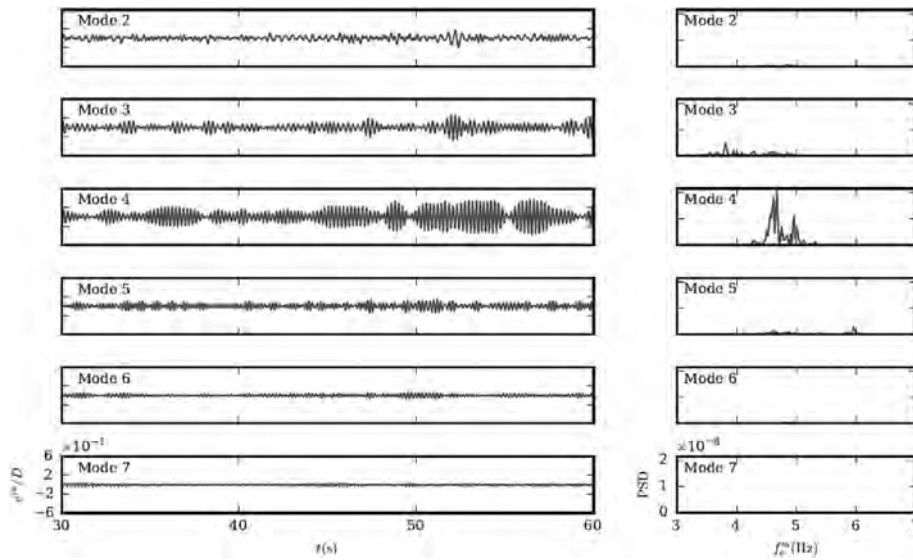

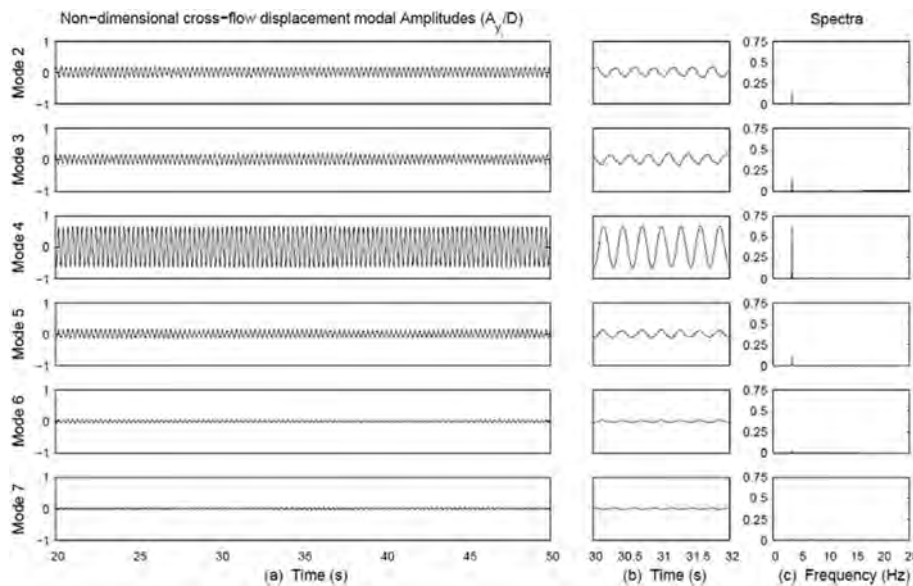**Fig. 6.** CF displacement modal amplitudes and power spectral density.

Fig. 7. CF displacement modal amplitudes and power spectral density from the experimental results of Huera-Huarte (2006).

experimental data of Huera-Huarte (2006) (see Fig. 9 (b)). The instantaneous color legend of the experiment is always the same because the experimental modal weight of each order is very stable. For the numerical study, although the vibration mode shape is the same, the amplitude is time variant. Therefore, the instantaneous color legend of the present study varies. This is because the numerical modal weight cannot remain constant all the time because of the turbulence.

3.4. In-line motion analysis

The CF vibration is around the initial position. Unlike the CF motion, the riser first reaches its equilibrium position, and then it vibrates around the position in the IL direction. Fig. 10 shows the IL mean displacement plotted against the relative elevation z/L. The red line represents the experimental results, and the blue line represents the results of this study. As shown in Fig. 10, the maximum displacement is not in the middle of the line because the displacement of the upper part of the riser (in still water) is smaller than the displacement of the lower part exposed to the current. The IL equilibrium position agrees well with the experimental

results. The value and location of the maximum IL displacement are listed in Table 5. The present study precisely predicts the location of the maximum displacement with an error of only 1.1%.

The rest of the analysis for the IL motion of the riser is performed as in the previous section. The IL modal amplitudes from the 5th to the 10th order are provided in Fig. 11. High consistency was achieved as compared with the experimental results of Huera-Huarte (2006), as shown in Fig. 12. The IL response predicted by the numerical method is entirely dominated by the 7th mode, which is consistent with the experimental data; it also presents the dominant 7th mode of the IL vibration. Fig. 11 shows few contributions from the modes on either side of the dominant 7th mode. The modal weight of the 7th mode is very stable and steady, and the modal weight of the 6th and 8th modes is much smaller than the 7th mode. The IL vibration is in the form of a standing wave.

An FFT is applied to obtain the IL displacement modal amplitude, which is used to explain the mechanism of the dominant mode. On the right of Fig. 11 is the power spectrum of each IL modal amplitude. The dominant 7th mode has the largest spectral densities; it has a frequency
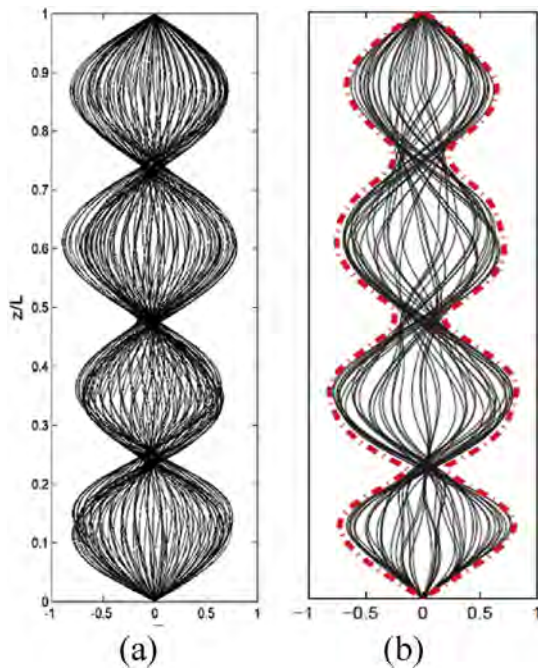
Fig. 8. CF deflected shapes of the riser.

of 9.032 Hz. This value is close to the 7th natural frequency. The IL vibration is excited by the drag imposed on the riser, and the CF vibration is excited by the lift. The frequency of the IL oscillation is about twice that of the CF direction because the drag frequency is approximately twice that of the lift. The change of natural frequency is non-linear. The natural

frequency increases slowly along with the increase of the top tension. Therefore, the 7th natural frequency is about twice that of the 4th order. It is easy to identify the mode shape from the instantaneous spatio-temporal plot of the non-dimensional IL response, as shown in Fig. 13. The numerical results agree well with the experimental data, as shown in Fig. 14. The single 7th mode is seen as the result of the nearly constant IL modal amplitudes plotted in Fig. 11.

3.5. Flow field analysis

The vortex-induced vibration of a long, flexible riser is excited by the flow field. Fig. 16 shows the lift and drag coefficients at the 15th slice, where the IL displacement is the largest. It is worth noting that the fluctuation range of the drag coefficient is larger than that of a fixed cylinder.

The time history of displacements corresponds to the time history of hydrodynamic coefficients. Fig. 15 depicts the IL and CF displacements of the 15th slice. The lift coefficient is very small in the initial 2.5 s; the corresponding CF displacement is also very small. The drag coefficient increases rapidly from the start. The drag coefficient begins to vibrate around this position to reach the equilibrium position, after approximately 4 s. The IL displacement correspondingly increases from the start and vibrates around the equilibrium position after 4 s. Generally speaking, the motion of the riser in the early stage is primarily in the IL direction. After reaching its IL equilibrium position, the vortex begins to shed alternatively from the riser. The motion of the riser is mainly manifested by the CF vibration at the IL equilibrium position. The consistency between the hydrodynamic force and the displacement illustrates the fluid-structure coupling effect. Fig. 17 depicts the contours of the instantaneous vorticity magnitude along the riser from the IL and CF views. At this Reynolds number, a 2S pattern is observed.
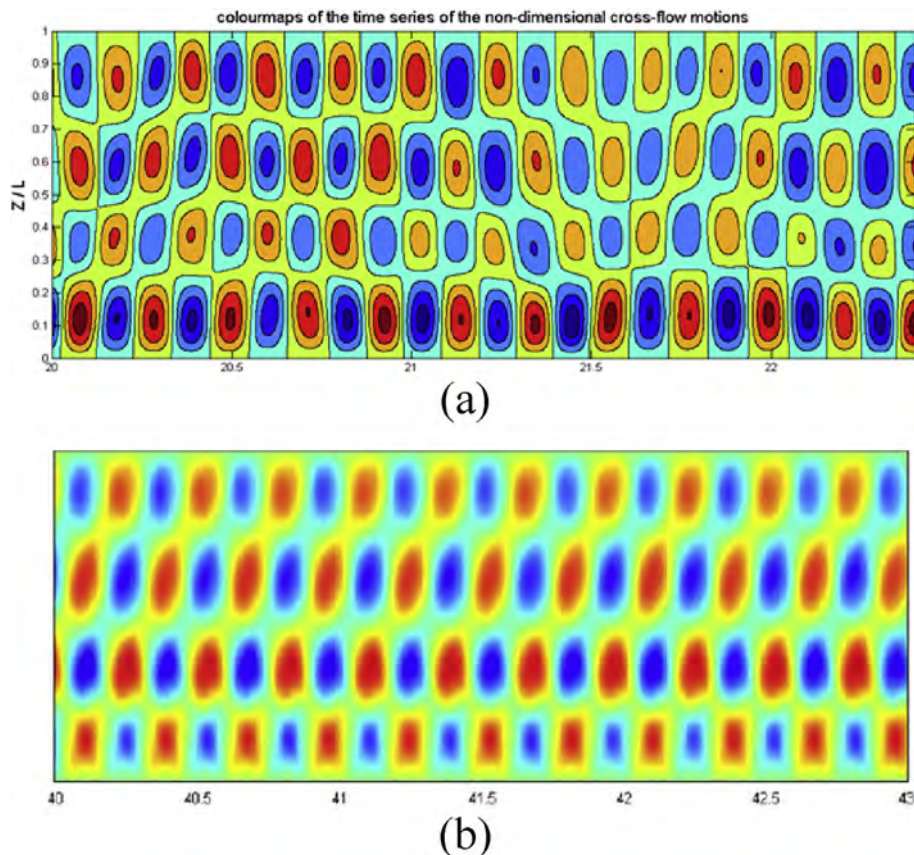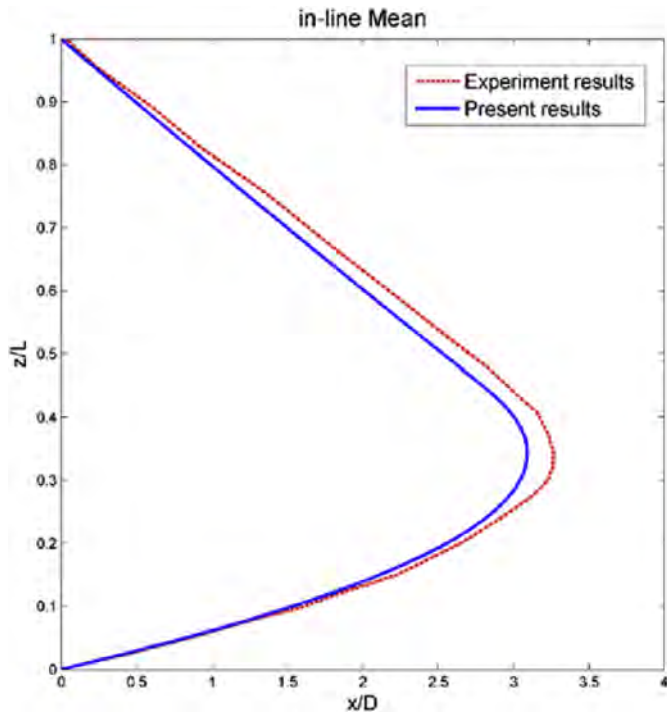

Fig. 9. Spatio-temporal plot of CF response.

Fig. 10. Mean IL displacement.

Table 5
Value and location of the max IL displacement.

	The max value of IL displacement	The location of the max value
Experiment	3.292 D	0.371 L
Present	3.072 D	0.367 L
Error/%	6.7	1.1

4. Parametric investigations

A series of parametric studies with varying parameters were further performed separately to investigate the effects of the top tension, the current velocity and the mass ratio.

4.1. Parametric analysis of current velocity

Three current velocities were considered in this section: $U = 0.2 \text{ ms}^{-1}$, 0.4 ms^{-1} and 0.6 ms^{-1}, where 0.6 ms^{-1} indicates the benchmark case for section 3. The main results for the different current velocities are listed in Table 6. It includes the maximum IL mean displacement ($\overline{x}_{\max}/D$), the location of the maximum IL mean displacement (z/L), the maximum IL RMS displacement, the maximum CF RMS displacement, the dominate IL mode and the dominate CF mode.

When the velocity is low, the vibration can be quite moderate. In the numerical simulation, the riser vibrated at the 2nd mode in the IL direction whereas in the CF direction, it vibrated at the 1st mode (see Figs. 18 and 19). Not only the dominant mode, but also the maximum mean displacement was considerably reduced (compared to the benchmark) from 3.072 to 0.389 times the riser diameter.

When the current velocity was increased to $U = 0.4 \text{ ms}^{-1}$, the riser pipe vibrated at the 5th mode in the IL direction and 3rd mode in the CF direction, as shown in Figs. 20 and 21. The maximum mean displacement was 0.910 times the riser diameter. With increasing current velocity, the maximum mean IL displacement increased, and the position of the maximum value became low. This is reasonable because drag increases with increasing current velocity. Furthermore, only the lower part of the pipe experienced current flow, this asymmetry played a significant role as the increase of the velocity, which resulted in a keep falling of the location of the maximum IL displacement. With larger current velocities, higher modes tend to be excited. This is because the natural frequency of the riser is not changed with the varying current velocity. Since the Strouhal number maintains at approximately 0.2 in a large range of Reynolds numbers. The Strouhal number is defined as $St = f_s D/U$. The vortex shedding frequency increases as the flow velocity increases. In other words, the vortex shedding frequency is proportional to the current velocity. The oscillatory frequency of nodes is equal to the vortex shedding frequency when lock-in happens. The natural frequency remains unchanged, and the oscillatory frequency increases with increased flow velocity. Therefore, the natural frequency order corresponding to the oscillatory frequency increases.

4.2. Parametric analysis of top tension

Three top tensions are considered: 1600 N, 1900 N and 2200 N; the benchmark is $T = 1600$ N. The dominant mode of $T = 1600$ N is the 4th mode in the CF direction. As presented in section 3, the amplitude of the 4th mode is greater than the amplitude of 3rd mode all the time. No jump
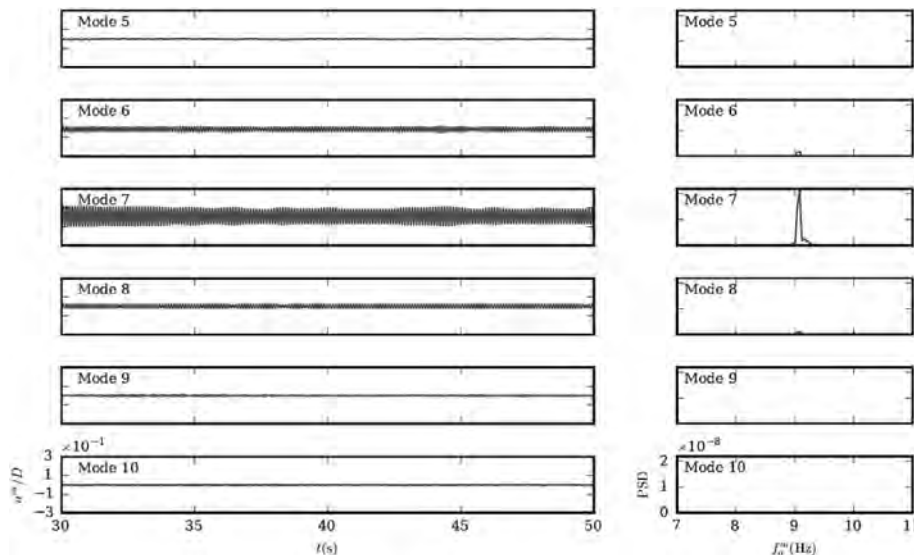

Fig. 11. IL displacement modal amplitudes and power spectral density.
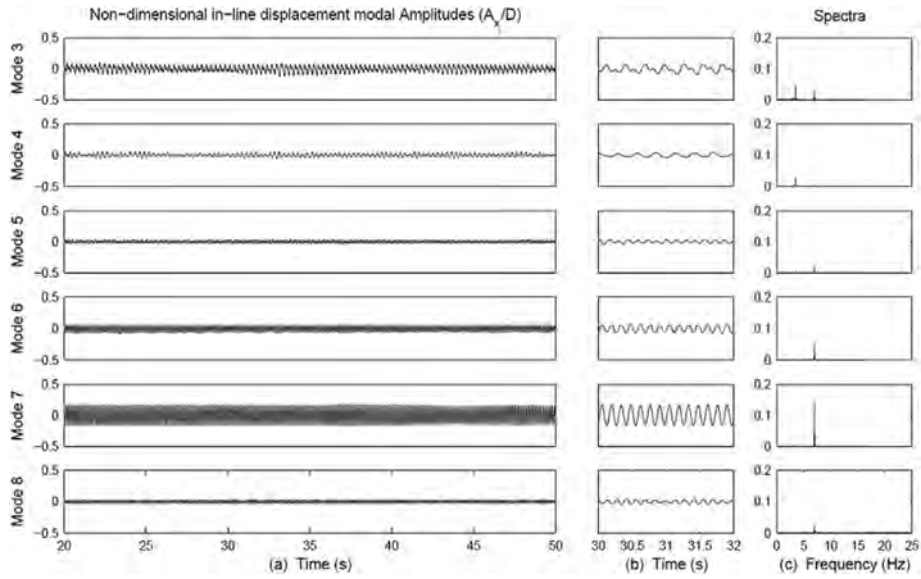
Fig. 12. IL displacement modal amplitudes and power spectral density from the experimental results of Huera Huarte (2006).

between multi-modes is present in the CF vibration; therefore, the mode shape is of a very stable 4th order. When the top tension is increased to 1900 N, the modal weight of the 3rd mode increases in the CF direction; at some interval, the weight of the 3rd mode becomes even larger than that of the 4th mode, which can be easily seen from Fig. 22. The 3rd mode carries a bigger weight when $T = 1900$ N than when $T = 1600$ N. Therefore, the mode shape sometimes exhibits the 3rd order. Most of the time, the mode shape is the unsteady 4th order. Fig. 23 is the spatio-temporal plot of the CF response, which shows the transition process between the 4th and 3rd modes when $T = 1900$ N. It indicates that the

dominant mode number begins to decrease with increasing top tension.

The above view of mode transition is also supported by the instantaneous deflected IL and CF shapes, as shown in the Fig. 24. The envelope

Fig. 15. Time history of IL and CF displacement.
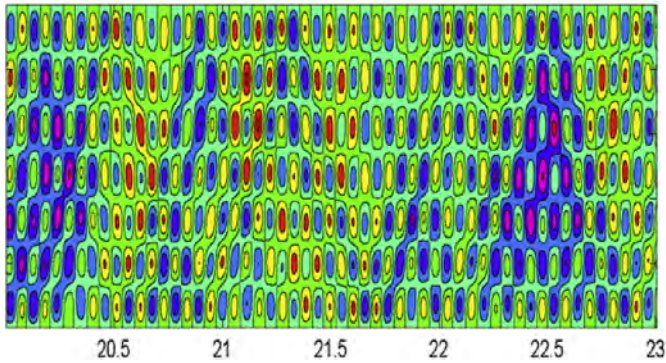
Fig. 13. Spatio-temporal plot of IL response.
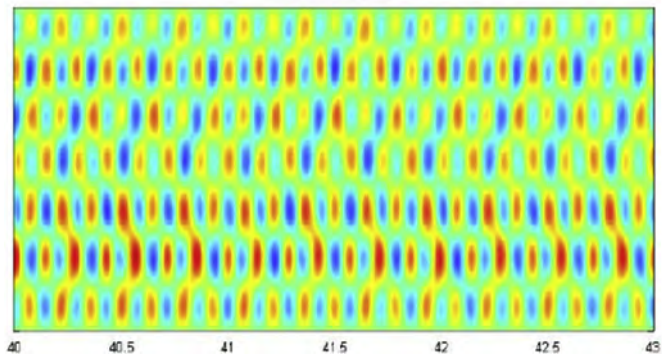
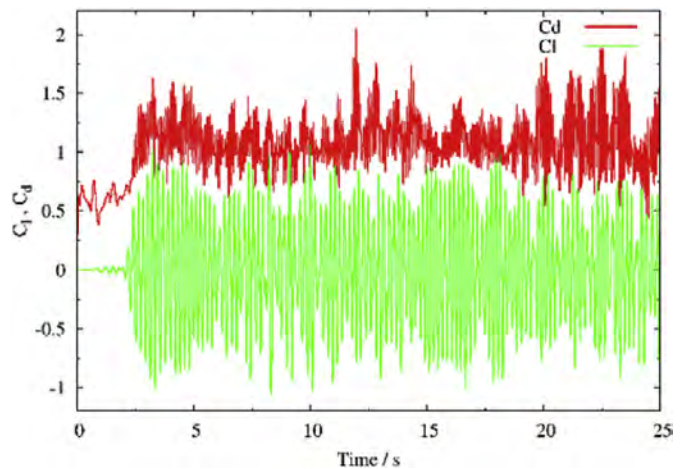**Fig. 14.** Spatio-temporal plot of IL response of Huera Huarte (2006).

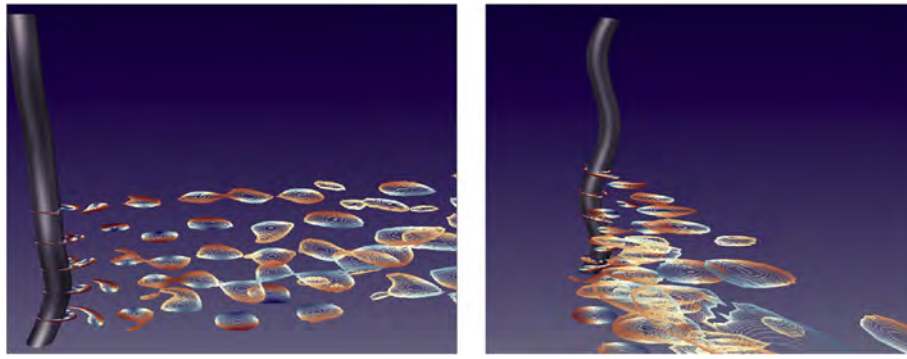**Fig. 16.** Time history of Cl and Cd.

Fig. 17. Vortex-shedding along riser from IL and CF view.

Table 6
VIV response with different flow velocity.

Flow velocity	$\overline{x}_{max}/D$	Location of $\overline{x}_{max}$	Max of x_{RMS}/D	Max of y_{RMS}/D	IL Mode	CF Mode
$U = 0.2$ m/s	0.389	0.381	0.157	0.834	2	1
$U = 0.4$ m/s	0.910	0.374	0.053	0.126	5	3
$U = 0.6$ m/s	3.072	0.367	0.177	0.561	7	4

of the IL vibration is very clear, and there is a distinct mode shape. Whereas the instantaneous deflected CF shape is not clear, and two mode shapes (the 3rd mode and the 4th mode) coexist in the envelop together.

When $T = 2200N$, the IL dominant mode is further reduced to the 6th mode while the CF vibration remains at the steady 3rd mode; this conforms with the tendency described above. Fig. 25 depicts the IL and CF instantaneous deflected shapes of the riser.

The main results for different top tensions are listed in Table 7. The VIV response of the riser follows the rule that the maximum IL mean value increases with the reduced top tension. This is reasonable because a large tension means a stronger restriction, which makes a large deformation impossible. The positions of these maximum values barely varied with the top tension because the current profile is not changed, and the asymmetric effect of riser arising from the non-uniform flow field is the same. As the top tension increases, the dominant IL mode decreased from the 7th order to the 6th order, and the dominant CF mode decreased from the 4th order to the 3rd order. The top tension does have an effect on the vibration of riser, but its effect is less significant than the flow velocity.

Modal analysis was conducted to clarify the mechanism. The first seven natural frequencies of various top tensions are listed in Table 8. It is evident that the top tension can alter the natural frequencies. The natural frequencies increased as the top tension increased.

As stated in Willden and Graham (2004), the vibration depends upon the proximity of the natural frequency to the Strouhal frequency or the oscillatory frequency when a lock-in occurs. If we match the natural frequencies in Table 8 with the oscillatory frequencies, we can easily find the most proximate natural frequency. The corresponding mode number can be exactly obtained from in Table 8. For instance, when $T = 2200$ N, the dominant frequency of IL vibration is 8.335 Hz (see Table 8), which is very close to the 6th order natural frequency 8.778 Hz. Therefore, the IL mode shape presents the 6th order. The rule is also applicable to the CF direction. The dominant frequency of CF vibration is 4.177 Hz, which is very close to the 3rd order natural frequency 4.342 Hz. Therefore, the CF mode shape presents the 3rd order. In addition, the dominant mode number in the IL direction is usually twice the size of the mode number in the CF direction because the excitation frequency for the IL vibration is approximately twice the Strouhal frequency.

We concluded that the increasing top tension could suppress the vibration in two ways—by restricting the mean IL displacement and by reducing the vibration mode. However, increasing the top tension to suppress vibrations can never be a perfect solution. Excessive top tension makes the axial stress increase accordingly, which can cause negative effect on the strength of riser. A very large axial stress will undoubtedly reduce the life expectancy of the riser, which is undesirable.
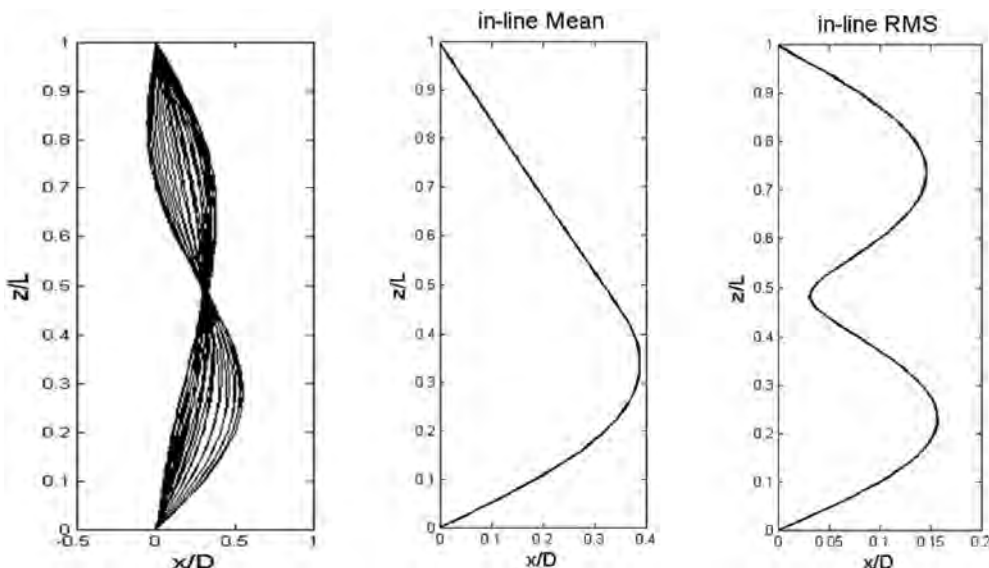

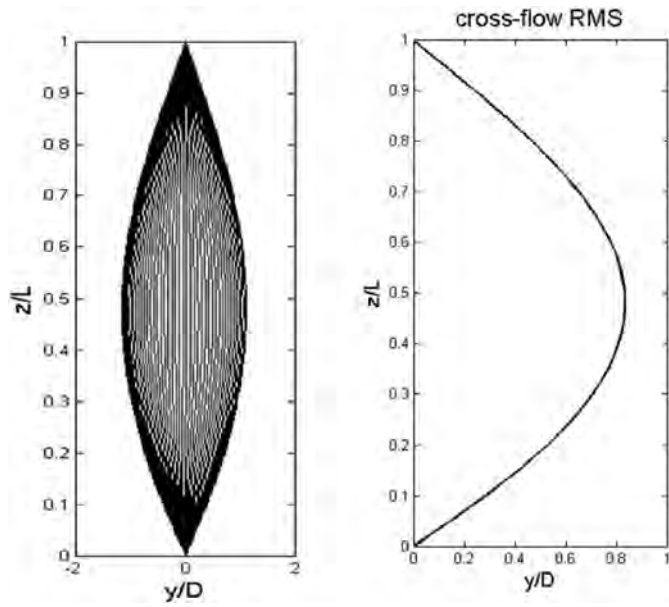**Fig. 18.** Deflected shapes, the mean and the standard deviation of IL displacement, $U = 0.2$ m/s.

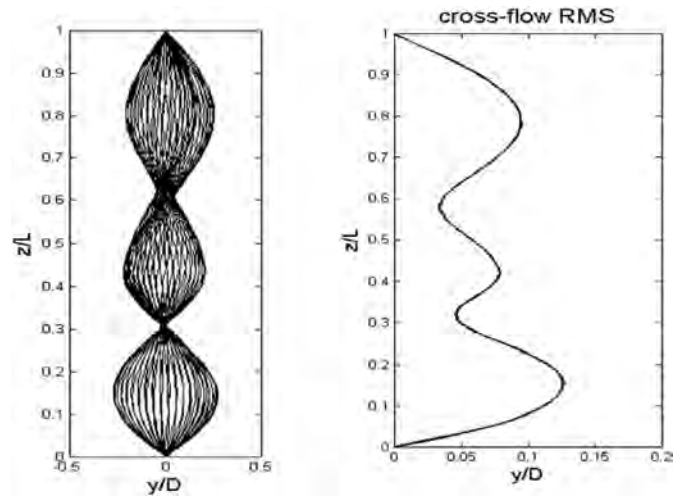Fig. 19. Instantaneous deflected shapes and the RMS CF displacement, $U = 0.2$ m/s.

4.3. Parametric analysis of mass ratio

Six mass ratios were simulated: $m^* = 2.0, 2.5, 3.0, 4.0, 5.0, 6.0$, where $m^* = 3.0$ indicates the benchmark for section 3.

The power spectral density of every node for $m^* = 2.0$ is shown in Fig. 26. The 3rd mode and 6th mode were attained for the CF and IL directions, respectively.

The root mean squares of the modal weight histories y_{rms}^m and x_{rms}^m are shown in Figs. 27 and 28, respectively, as a function of each mode's natural frequency normalized upon the Strouhal frequency of the stationary pipe at the same Reynolds number, f_s. The cases in this section are more than that in the study of parametric analysis of flow velocity and top tension. Consequently, the specific mode number for different mass ratio are not studied separately. Alternatively, as is done in this section,

Fig. 21. Instantaneous deflected shapes and the RMS CF displacement, $U = 0.4$ m/s.

all the modal responses are put together to be studied. In addition to macro law, we reached a more extensive and deeper analysis due to the new comparison method.

The two figures show that all of the test cases respond multi-modally in both directions, with each simulated response characterized by a response envelope. The envelope extends over several modes and is centered on a single dominant mode. However, we do not rule out the case where two adjacent modes are of similar weight. Changing m^* changes the pipe's natural frequencies and mode shapes, that is, the natural frequency of a specific mode becomes more closely spaced with increasing m^*. This conclusion can be drawn directly from Fig. 27. All the cases from $m^* = 2.0$ to $m^* = 6.0$ are drawn to the 10th mode; the natural frequency for $m^* = 2.0$ is about twice the natural frequency for $m^* = 6.0$.

As shown by Lie and Kaasen (2006), when a lock-in occurs, vortices are shed at the actual oscillatory frequency rather than at the Strouhal frequency, whereas the oscillatory frequency may not be exactly equal to the expected natural resonant frequency. Willden and Graham (2004) mentioned that the vortex shedding frequency was found to occur at the Strouhal frequency or slightly below it.
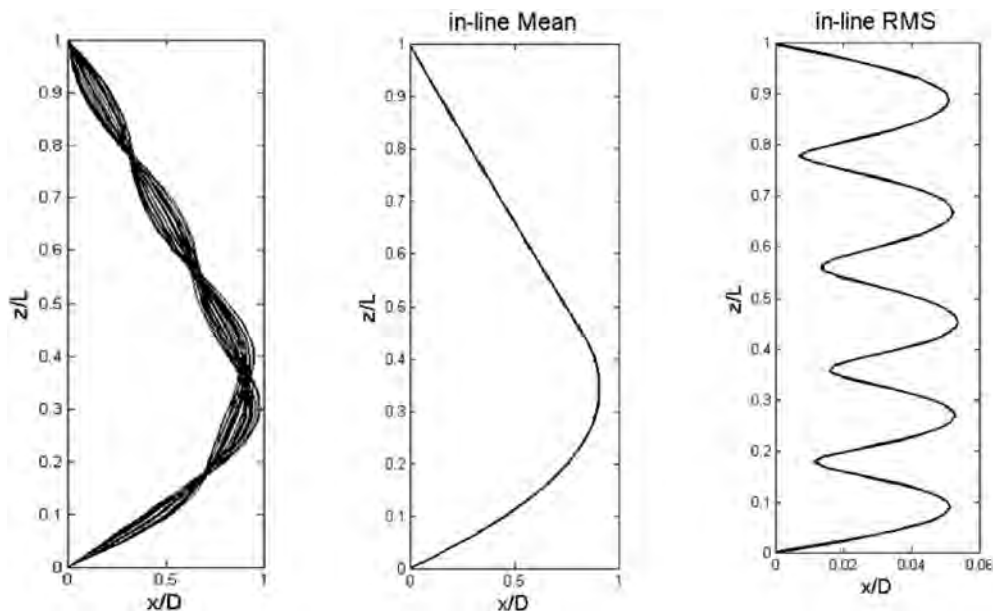

Fig. 20. Instantaneous deflected shapes, the mean and the RMS IL displacement, $U = 0.4$ m/s.
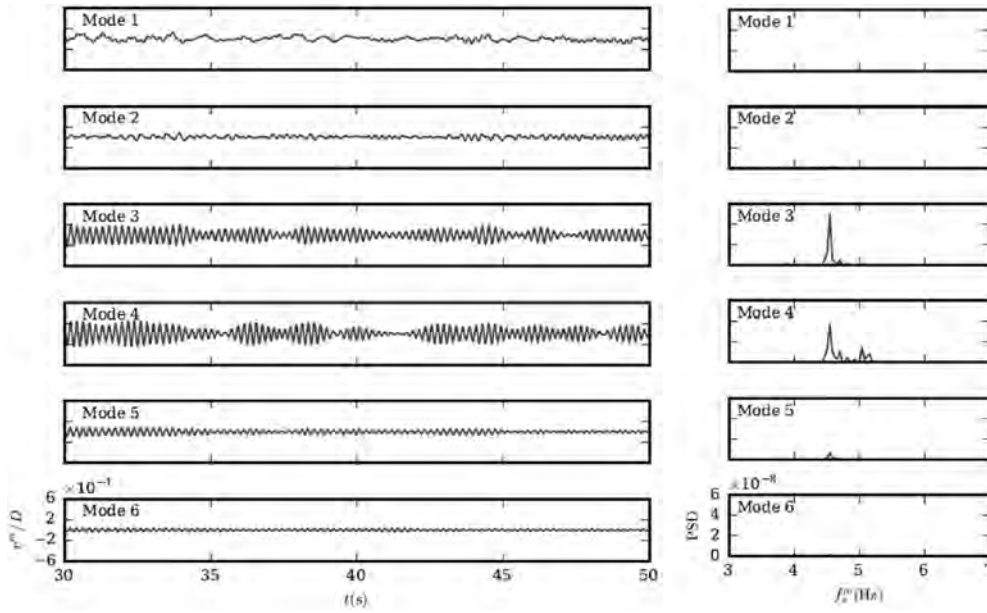
Fig. 22. Power spectral density of modal weight of CF displacement for $T = 1900$ N.

However, a general tendency can still be found from Fig. 27. When focusing on the dominant mode, it can be clearly seen that the natural frequency of most of them are slightly below the Strouhal frequency. The
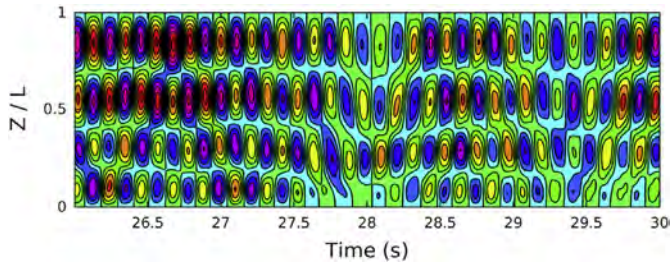
dominant mode number tends to increase with the mass ratio, as shown in Table 9. When the mass ratio increased from 2 to 2.5, the peak value also increased whereas the dominant mode number remained unchanged. The dominant mode changes from the mass ratio of 2.5–3, whereas the peak value decreases. A mode transition happens between these two cases. For the mass ratio of 2.5, the lock-in is mainly confined to the 3rd mode, and the 4th mode takes place for the mass ratio 3. For the mass ratios of 4 and 5, the peak value goes as high as the peak values
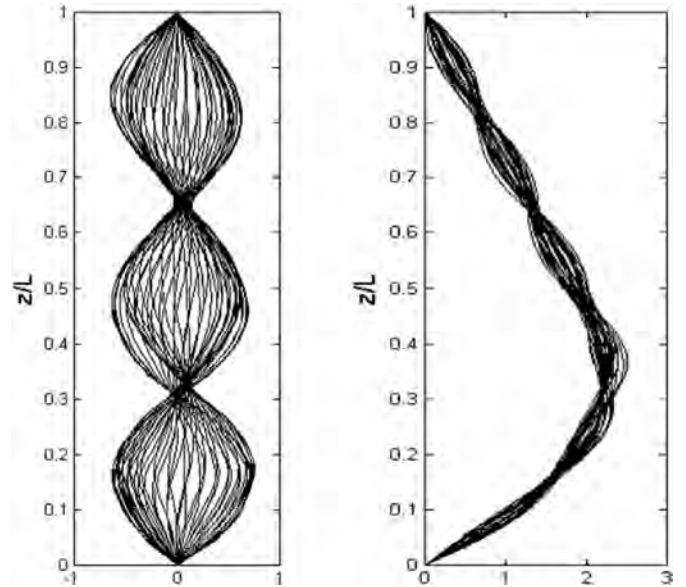

Fig. 23. Spatio-temporal plot of CF response, $T = 1900$N.

Fig. 25. Instantaneous deflected IL and CF shapes of the riser, $T = 2200$N (left: CF, right: IL).

Table 7
VIV response with different top tension.

Top tension	$\overline{x}_{max}/D$	Location of $\overline{x}_{max}$	Max of x_{RMS}/D	Max of y_{RMS}/D	IL Mode	CF Mode
$T = 1600$N	3.072	0.367	0.177	0.561	7	4
$T = 1900$N	2.440	0.352	0.111	0.243	7	3–4
$T = 2200$N	2.282	0.367	0.150	0.484	6	3

Fig. 24. Instantaneous deflected IL and CF shapes of the riser, $T = 1900$N (left: CF, right: IL).

Y. Duanmu et al.

Table 8
Natural frequency with different top tension.

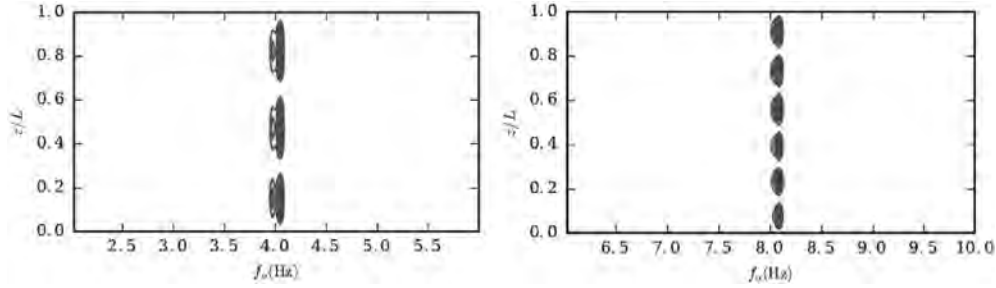| T (N)	f_{n1}	f_{n2}	f_{n3}	f_{n4}	f_{n5}	f_{n6}	f_{n7}	IL dominant frequency	CF dominant frequency
1600	1.224	2.452	3.688	4.936	6.201	7.487	8.796	9.032	4.556
1900	1.336	2.675	4.023	5.381	6.755	8.147	9.561	8.736	4.344
2200	1.443	2.889	4.342	5.805	7.283	8.778	10.29	8.335	4.177

Fig. 26. Power spectral density contour of CF and IL displacement for $m^* = 2.0$.
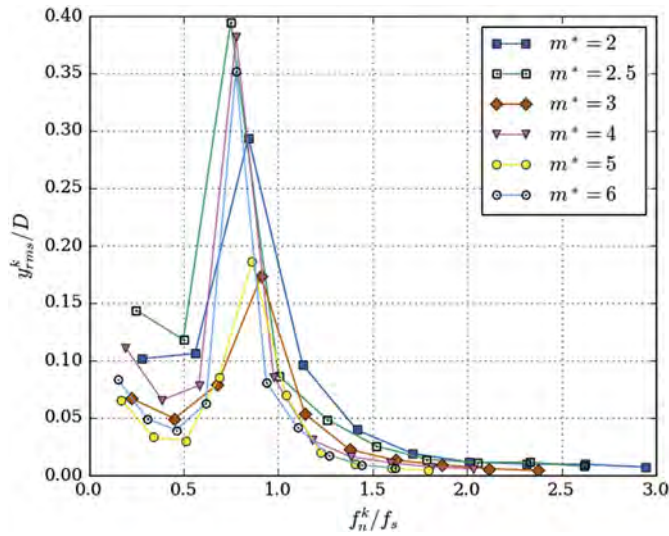

Fig. 27. CF modal RMS vibration amplitudes, y_{rms}^k/D, as a function of modal natural frequencies normalized by the Strouhal frequency f_n^k/f_s, with different mass ratio.
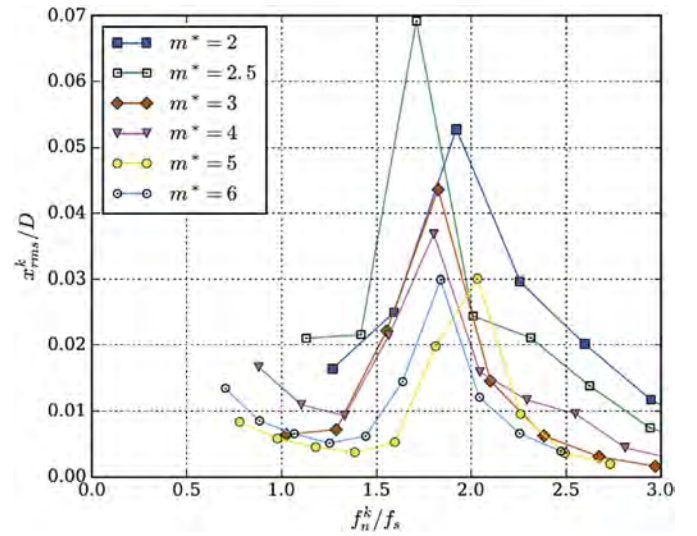

Fig. 28. IL modal RMS vibration amplitudes, x_{rms}^k/D, as a function of modal natural frequencies normalized by the Strouhal frequency, f_n^k/f_s, with different mass ratio.

for the mass ratio of 2.5. There occurs a sudden drop in the peak value again for the mass ratio of 5. A transition from the 4th mode to the 5th mode occurs again, which confirms our prediction. Consequently, we can conclude that the dominant mode number tends to increase with the mass ratio, whereas the amplitude of the dominant mode mainly depends on the proximity of the natural frequency to the vortex shedding frequency. A sudden drop of peak value may happen for mode transitions.

In Fig. 28, the drawn modes start from the 4th mode. The dominant modes for IL vibrations are more sensitive to the natural frequencies. Anyway, the conclusions we draw from Fig. 27 can also apply to Fig. 28. Generally speaking, the dominant mode increases with the mass ratio. Furthermore, the natural frequency of the dominant mode for IL vibrations largely remains twice that in the CF direction. A further comparison between Figs. 27 and 28 indicates that the width of the response envelope for IL vibrations is larger than that of CF vibrations. This can be reasonable because we expect more modes to be involved in the higher mode number vibrations.

5. Discussion

A common concern in VIV study is how the response changes with

reduced velocity. The numerical results obtained previously in section 4 are analyzed now to further study the trend of the mode, amplitude and curvature with reduced velocity. The discussion is based on the following data processing method.

Overall indications of the magnitudes of IL and CF responses are provided by the root mean square values over z of the standard deviations of x and y with respect to time. This is defined by

$$\sigma_x^{rms} = \sqrt{\frac{1}{L}\int_0^L \frac{1}{T}\int_0^T [x(z,t) - \bar{x}(z)]^2 dt dz},$$

$$\sigma_y^{rms} = \sqrt{\frac{1}{L}\int_0^L \frac{1}{T}\int_0^T [y(z,t) - \bar{y}(z)]^2 dt dz},$$

where $\bar{x}(z,t)$ and $\bar{y}(z,t)$ are the time-averaged IL displacement and CF displacement, respectively. The time-averaged CF displacement $\bar{y}(z,t)$ is expected to be zero. The integration in time is carried out over an interval T in which the velocity is constant; in general, this is the last 30 s of the 60 s duration of each test.

The root mean square values of the standard deviations of the IL and CF curvatures $\sigma_{c_x}^{rms}$ and $\sigma_{c_y}^{rms}$ can similarly be defined as

Table 9
Dominant VIV mode with different mass ratio.

m*	IL mode	CF mode
2	3	6
2.5	3	6
3	4	7
4	4	8
5	5	10
6	5	10

$$\sigma_{c_x}^{rms} = \sqrt{\frac{1}{L}\int_0^L \frac{1}{T}\int_0^T [c_x(z,t) - \overline{c}_x(z)]^2 dt dz}$$

$$\sigma_{c_y}^{rms} = \sqrt{\frac{1}{L}\int_0^L \frac{1}{T}\int_0^T [c_y(z,t) - \overline{c}_y(z)]^2 dt dz}$$

The RMS value of the standard deviation, the maximum attainable value of displacement and the oscillatory frequency are plotted in Figs. 29 and 30 as functions of the reduced velocity $V/(f_1 D)$. Here, V is the flow velocity, and D is the cylinder diameter. The frequency f_1 is the riser's natural frequency in still water in the fundamental mode, which is obtained from FEM with the corresponding top tension.

In Fig. 29, the standard deviations of displacements appear to be quite widely scattered with most points in the range of 0.04 and 0.12 diameters for IL motion and between 0.1 and 0.3 diameters for the CF direction. However, as will be seen below, this is a consequence of systematic changes that take place as the reduced velocity passes through the lock-in range for successive modes. This result suggests that the modal content has a major effect on the overall amplitude of the riser's response, which is therefore quite sensitive to small changes in the reduced velocity.

The IL and CF curvatures are of similar magnitudes. The fact that the curvatures increase approximately with $(V/f_1 d)^2$ is consistent with the interpretation that the oscillations occur at an approximately constant amplitude and at a mode number that increases linearly with reduced velocity.

The time-averaged displacement of the riser in the IL direction followed the same form in all cases. Increasing the velocity of the current has the effect of increasing the drag, thereby increasing the modal frequencies and the maximum mean IL offset x_{max}. The modal frequencies, such as f_1, are approximately proportional to the square root of the
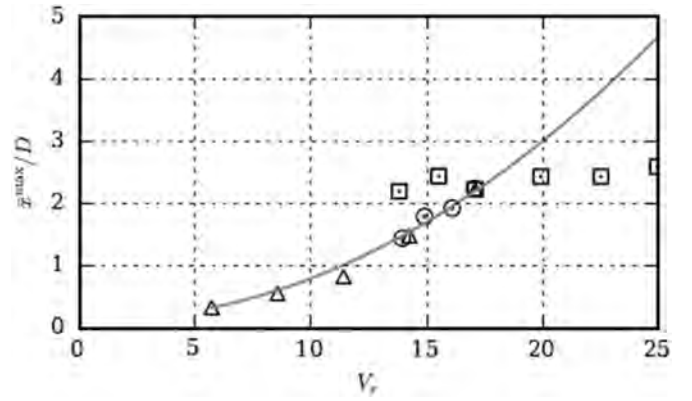

Fig. 30. Tendency x_{max}, □ indicates cases with various mass ratios m^*, while ○ indicates that with various top tensions T and △ indicates that with various current velocities V.

tension; therefore, it follows that if the drag coefficients are constant, the maximum mean offset would be proportional to the square of the reduced velocity $\overline{x}_{max}/D = C(V/f_1 D)^2$ with C independent of the initial still water tension. The results of the maximum mean offsets for all tests (plotted together in Fig. 30) are clustered around this relationship. However, the maximum mean offsets depart from this relationship slightly, which suggests that there are significant changes in drag coefficients associated with mode switching.

6. Conclusions

We made comprehensive calculations of the vortex-induced vibrations of a 13.12 m long model vertical tension riser having a diameter of 28 mm and a mass ratio of 3.0. The tests were carried out in a step current consisting of a uniform flow over the bottom 45% of the riser, whereas the remainder was in still water. A good agreement between the numerical and experimental results showed that the self-developed solver is reliable. Good quality results have been obtained for the frequencies and amplitudes of responses with the 4th and 7th modes in transverse and IL directions, respectively. The numerically predicted mean IL displacements have good consistency with the experimental result with an approximate error of only 1%.
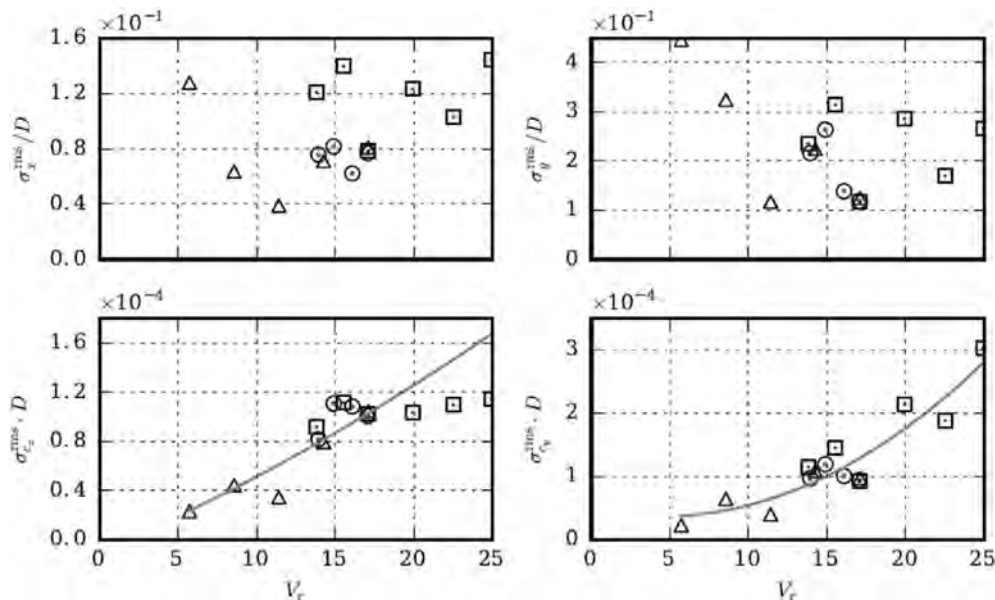

Fig. 29. Tendency, □ indicates cases with various mass ratios m^*, while ○ indicates that with various top tensions T and △ indicates that with various current velocities V.

In the following study, we carried out a series of numerical simulations of VIVs of a vertical tension riser. The current velocity, top tension and mass ratio were investigated in detail to understand their effects on the VIV responses of long flexible risers. The parameters were studied separately to obtain some laws pertaining to them. For example, it was found that the maximum IL mean displacement decreases with the increase of top tension. However, the location is almost unchangeable in any case. The trend of mode order reduction is obtained as the top tension increases. The relationship between the natural frequency and oscillating frequency was intensely investigated to explain the reason for the occurrence of the dominant mode.

Finally, the previous results of all the cases were analyzed to study the VIV responses for the reduced velocity. Our understanding of the VIVs of long flexible risers has benefited considerably from the fact that a large number of tests were carried out. In this study, the amplitude of the response in each mode grew monotonically as the reduced velocity increased through its lock-in range. Generally, the overall response of the riser included significant contributions from two or more modes, and each combination persisted over a range of reduced velocities. However, these ranges overlapped so that a given reduced velocity could give rise to more than one pattern of modal contributions. These remarks apply equally to the IL and CF motions, and the steps in VIV responses in both directions are clearly linked. The standing wave or travelling wave responses were captured for different reduced velocities.

Acknowledgements

References

Borazjani, I., Sotiropoulos, F., 2009. Vortex-induced vibrations of two cylinders in tandem arrangement in the proximity-wake interference region. J. Fluid Mech. 621, 321–364.

Chaplin, J., Bearman, P., Cheng, Y., Fontaine, E., Graham, J., Herfjord, K., Huarte, F.H., Isherwood, M., Lambrakos, K., Larsen, C., et al., 2005a. Blind predictions of laboratory measurements of vortex-induced vibrations of a tension riser. J. Fluid Struct. 21 (1), 25–40.

Chaplin, J., Bearman, P., Huarte, F.H., Pattenden, R., 2005b. Laboratory measurements of vortex-induced vibrations of a vertical tension riser in a stepped current. J. Fluid Struct. 21 (1), 3–24.

Chen, W., Li, M., Zheng, Z., Tan, T., 2012. Dynamic characteristics and VIV of deepwater riser axially varying structural properties. Ocean Eng. 42, 7–12.

Duan, M.Y., Wan, D.C., 2016a. Large eddy simulation of flow around the cylinders with different aspects. Chin. J. Hematol. 31 (3), 295–302.

Duan, M.Y., Wan, D.C., Xue, H.X., 2016. Prediction of response for vortex-induced vibrations of a flexible riser pipe by using multi-strip method. In: Proceedings of the Twenty-sixth International Ocean and Polar Engineering Conference(ISOPE2016), Rhodes, Greece, pp. 1065–1073.

Huang, K., Chen, H.C., Chen, C.R., 2011. Numerical scheme for riser motion calculation during 3D VIV simulation. J. Fluid Struct. 27, 947–961.

Huera Huarte, F.J., 2006. Multi-mode Vortex-induced Vibrations of a Flexible Circular Cylinder. PhD thesis. the University of London.

Huera-Huarte, F., Bearman, P., Chaplin, J., 2006. On the force distribution along the axis of a flexible circular cylinder undergoing multi-mode vortex-induced vibrations. J. Fluid Struct. 22 (6), 897–903.

Huera-Huarte, F., Bearman, P., 2009a. Wake structures and vortex-induced vibrations of a long flexible cylinder part1: dynamic response. J. Fluid Struct. 25 (6), 969–990.

Huera-Huarte, F., Bearman, P., 2009b. Wake structures and vortex-induced vibrations of a long flexible cylinder part2: drag coefficients and vortex modes. J. Fluid Struct. 25 (6), 991–1006.

Lie, H., Kaasen, K., 2006. Modal analysis of measurements from a large-scale viv model test of a riser in linearly sheared flow. J. Fluid Struct. 22 (4), 557–575.

Rendall, T.C.S., Allen, C.B., 2008. Unified fluid-structure interpolation and mesh motion using radial basis functions. Int. J. Numer. Meth. Eng. 74 (104), 1519–1559.

Srinil, N., 2010. Multi-mode interactions in vortex-induced vibrations of flexible curved/straight structures with geometric nonlinearities. J. Fluid Struct. 26 (7), 1098–1122.

Wang, E., Xiao, Q., 2016. Numerical simulation of vortex-induced vibration of a vertical riser in uniform and linearly sheared currents. Ocean Eng. 121, 492–515.

Willden, R., Graham, J., 2001. Numerical prediction of VIV on long flexible circular cylinders. J. Fluid Struct. 15 (3), 659–669.

Willden, R., Graham, J.M.R., 2004. Multi-modal vortex-induced vibrations of a vertical riser pipe subject to a uniform current profile. Eur. J. Mech. B Fluid 23 (1), 209–218.

Willden, R., Graham, J., 2006. Three distinct response regimes for the transverse vortex-induced vibrations of circular cylinders at low Reynolds numbers. J. Fluid Struct. 22 (6), 885–895.

Zhang, K., et al., 2017. Numerical simulation of vortex induced vibrations of a flexibly mounted wavy cylinder at subcritical Reynolds number. Ocean Eng. 133 (15), 170–181.

Zhao, W.W., Wan, D.C., 2016a. Numerical study of 3D flow past a circular cylinder at subcritical Reynolds number using SST-DES and SST-URANS. Chin. J. Hematol. 31 (1), 1–8.

Zhao, W.W., Wan, D.C., 2016b. Detached-eddy simulation of flow past tandem cylinders. Appl. Math. Mech. 37 (12), 1272–1281.